Interaction between Multiple Current Sheets and a Shock Wave: 2D Hybrid Kinetic Simulations

M. Nakanotani[1] , G. P. Zank[1,2] , and L.-L. Zhao[1]

[1] Center for Space Plasma and Aeronomic Research (CSPAR), University of Alabama in Huntsville, Huntsville, AL 35805, USA; mn0052@uah.edu
[2] Department of Space Science, University of Alabama in Huntsville, Huntsville, AL 35899, USA
Received 2021 August 31; revised 2021 September 30; accepted 2021 October 7; published 2021 December 1

Abstract

Particle acceleration behind a shock wave due to interactions between magnetic islands in the heliosphere has attracted attention in recent years. The downstream acceleration may yield a continuous increase of particle flux downstream of the shock wave. Although it is not obvious how the downstream magnetic islands are produced, it has been suggested that current sheets are involved in the generation of magnetic islands due to their interaction with a shock wave. We perform 2D hybrid kinetic simulations to investigate the interaction between multiple current sheets and a shock wave. In the simulation, current sheets are compressed by the shock wave and a tearing instability develops at the compressed current sheets downstream of the shock. As the result of this instability, the electromagnetic fields become turbulent and magnetic islands form well downstream of the shock wave. We find a "post-cursor" region in which the downstream flow speed normal to the shock wave in the downstream rest frame is decelerated to $\sim 1 V_A$ immediately behind the shock wave, where V_A is the upstream Alfvén speed. The flow speed then gradually decelerates to 0 accompanied by the development of the tearing instability. We also observe an efficient production of energetic particles above $100\, E_0$ during the development of the instability some distance downstream of the shock wave, where $E_0 = m_p V_A^2$ and m_p is the proton mass. This feature corresponds to Voyager observations showing that the anomalous cosmic-ray intensity increase begins some distance downstream of the heliospheric termination shock.

Unified Astronomy Thesaurus concepts: Space plasmas (1544); Solar magnetic reconnection (1504); Interplanetary shocks (829)

1. Introduction

Current sheets are commonly observed in the heliosphere, from the inner heliosphere (Lavraud et al. 2020) to around 5 au (Zhao et al. 2019a), and beyond the distance to the outer heliosphere (Richardson et al. 2016). Since the magnetic axis of the Sun tilts with respect to the rotation axis of the Sun, the solar magnetic field flaps around the solar equator and forms a wavy shape, the so-called heliospheric current sheet. The heliospheric current sheet is advected by the solar wind and finally reaches the heliospheric termination shock (HTS). Current sheets can generate magnetic islands via magnetic reconnection (Biskamp 1986, 1996). Kinetic simulations show that current sheets can be unstable against tearing and drift-kink instabilities depending on their thickness, and the unstable current sheets trigger magnetic reconnection (Gingell et al. 2015; Burgess et al. 2016a; Gingell et al. 2017). The triggered magnetic reconnection forms magnetic islands in the system, which then interact with each other to develop a turbulent flow (Burgess et al. 2016a).

Magnetic islands/turbulence, however they are generated, are expected to play an important role in the acceleration and transport of energetic particles behind a shock wave. Voyager observations have found a gradually increasing flux of anomalous cosmic rays (ACRs) behind the heliospheric termination shock and then well into the inner heliosheath (Decker et al. 2005; Stone et al. 2005, 2008; Cummings & Stone 2013). In this paper, we focus on the observed enhancement of the ACR intensity behind the heliospheric termination shock, within about 1 au. The origin of the other observed ACR intensity, which continues to increase over 10 au, has been discussed in McComas & Schwadron (2006). Zank et al. (2015) and le Roux et al. (2016) modeled

particle acceleration by downstream magnetic reconnection combined with diffusive shock acceleration. The model successfully explained Voyager 2 observations of a continuous increase in the ion intensity behind the heliospheric termination shock (Zank et al. 2015; Zhao et al. 2018, 2019b). Zhao et al. (2019a) identified magnetic islands downstream of the termination shock. Besides the termination shock, similar events showing a gradual increase of ion intensity behind a shock wave have been found at around 1 and 5 au (Adhikari et al. 2019; Zhao et al. 2019a).

Investigations into the evolution of multiple current sheets using self-consistent kinetic simulations have been presented. Gingell et al. (2015) and Burgess et al. (2016a) performed 3D hybrid simulations of multiple current sheets, finding that tearing and drift-kink instabilities plays a role in the evolution of turbulence from multiple current sheets. Burgess et al. (2016a) found that the turbulence developed a power-law feature that is induced by magnetic reconnection in the later stage of the simulation. Furthermore, the presence of pick-up ions (PUIs) does not change the behavior of the turbulence. No evident PUI acceleration is observed in the simulation. Full particle-in-cell (PIC) simulations have also been conducted for a system of multiple current sheets (Drake et al. 2010; Schoeffler et al. 2011; Du et al. 2020). Drake et al. (2010) found that particles, especially PUIs, can be effectively accelerated due to the coalescence of magnetic islands induced by magnetic reconnection at the current sheets (Drake et al. 2006; Oka et al. 2010; Du et al. 2018). Detailed theories have subsequently been developed to describe the transport and acceleration of charged particles in a turbulent environment of dynamically interacting magnetic islands (Zank et al. 2014; le Roux et al. 2015). Zank et al. (2014, 2015) and le Roux et al.

(2015, 2016) showed that power-law distributions can result from particle acceleration by multiple magnetic islands or flux ropes.

Although there have been several studies about the generation of magnetic islands in multiple current sheet systems, the interaction of a shock wave and multiple current sheets is not well understood for shock waves in the heliosphere. Tsubouchi & Matsumoto (2005) performed 1D hybrid simulations of the interaction between a shock wave and a single current sheet/ rotational discontinuity. Since their simulation is 1D, magnetic reconnection does not occur. Giacalone & Burgess (2010) used 2D hybrid kinetic simulations to investigate the formation of hot flow anomalies due to the interaction between the termination shock and heliospheric current sheets. Since the direction of the magnetic field consisting of a current sheet upstream is out of the plane, magnetic reconnection is prohibited. The interaction between a shock wave and multiple current sheets has been considered in a relativistic pair plasma using full PIC simulations (Lyubarsky 2005; Nagata et al. 2008; Sironi & Spitkovsky 2011; Lu et al. 2021). Such an interaction for a nonrelativistic ion–electron plasma has not yet been explored.

In this paper, we report a self-consistent calculation of a shock interacting with multiple current sheets using a 2D hybrid kinetic simulation for nonrelativistic shock waves. Since energetic particles can be efficiently accelerated in multiple current sheets (Drake et al. 2010), it is expected that a shock wave might accelerate incoming particles and that these accelerated particles could be further energized downstream by interacting with multiple current sheets. The paper is organized as follows. In Section 2, we describe the simulation method and the initial condition. Simulation results are shown in Section 3. The last section provides a summary and discussion. Since current sheets are an integral part of magnetized turbulence, appearing as coherent structures, this work is related to studies of the interaction of shocks with turbulence as discussed by, e.g., Guo et al. (2021) and Trotta et al. (2021).

2. 2D Hybrid Kinetic Simulation

In this study, we use a 2D hybrid kinetic simulation in which ions and electrons are treated as a superparticle and a massless fluid, respectively. We consider a single-ion species plasma of protons and electrons. Our simulation scheme is based on the Current Advance Method-Cyclic Leapfrog (CAM-CL) algorithm (Matthews 1994). The only difference is that we advance particles using the standard Buneman–Boris algorithm, which conserves particle energy well. Hybrid simulations are suitable to investigate ion-scale kinetic physics and ion acceleration since ion velocity distribution functions are resolved using superparticles.

A shock wave is produced by the injection method. A plasma is injected from the left boundary and hits the rigid wall at the right boundary. It reflects off of the wall and interacts with the incoming plasma to form a shock wave. In this arrangement, the simulation frame is the downstream rest frame and the shock wave propagates leftward. The injection method has been widely used to produce shock waves in hybrid simulations (e.g., Winske & Omidi 1996; Giacalone & Ellison 2000; Burgess et al. 2016b).

We also inject current sheets from the left boundary, which are advected by the plasma. The configuration of the current sheets is given by

$$B_x = 0; \quad (1)$$

$$B_y = B_0 \tanh\left[\frac{1}{\delta} \cos\left\{ \frac{2\pi(x + V_0 t)}{\lambda} \right\} \right]; \quad (2)$$

$$B_z = \sqrt{B_0^2 - B_y^2} \, \mathrm{sign}\left(\sin\left\{ \frac{2\pi(x + V_0 t)}{\lambda} \right\} \right), \quad (3)$$

where V_0 is the speed of the injected plasma, and δ and λ determine the thickness of the current sheets and the separation between them, respectively. The upstream plasma density and temperature are uniform. The structure satisfies the force-free condition (Bobrova et al. 2001; Nishimura et al. 2003; Burgess et al. 2016a; Fan et al. 2016; Le et al. 2016), and the upstream magnetic field reversal across current sheets conserves the magnitude of the magnetic field. The angle between the current sheets and the shock normal is perpendicular. The advected current sheets eventually interact with the shock wave.

The simulation parameters used in this study are as follows: injection speed $V_0 = 4V_{A0}$; plasma beta $\beta_p = 0.5$ for protons and $\beta_e = 0.1$ for electrons. These parameters are commonly found in the solar wind. We found that increasing the injection speed causes severe nonphysical oscillations at a current sheet in the CAM-CL code. Therefore, we chose a relatively small injection speed to avoid spurious oscillations. This can be suppressed by introducing a flux limiter for the magnetic induction equation (Matsumoto et al. 2012). The simulation box size is $L_x \times L_y = 1000 \times 102.4 c/\omega_p$, the grid size is $\Delta x = \Delta y = 0.2(c/\omega_p)$, and the time step is $\Delta t = 0.01\Omega_c^{-1}$. We choose $\delta = 0.2$ and $\lambda = 80c/\omega_p$, ensuring that the width and the separation of current sheets are larger than the ion skin depth c/ω_p and the gyroradius upstream of the shock, respectively. Here, V_{A0} is the Alfvén speed defined from the upstream plasma, c/ω_p is the upstream ion skin depth, where c is the speed of light, and ω_p is the proton plasma frequency, and Ω_c is the upstream proton cyclotron frequency. We set 200 particles per cell. This number of particles in the simulation should be sufficient to discuss distributions for energetic particles and is comparable with other studies of particle acceleration at shock waves (Su et al. 2012; Giacalone et al. 2021). We note that the present system is longer than our previous calculation (Nakanotani et al. 2020).

The following units are used in the paper unless otherwise stated: time, length, speed, magnetic fields, plasma density, and energy will be normalized by Ω_c, c/ω_p, V_{A0}, B_0, the upstream plasma density, and $m_p V_A^2$, where m_p is the proton mass.

3. Results

Figure 1 is a snapshot of the magnitude of the magnetic fields $|B|$ and the magnetic field components B_x, B_y, B_z from top to bottom at $T = 400$. The resultant shock speed is $1.7V_{A0}$ and the compression ratio for the shock is ~ 2.5. The shock wave is located at $X \sim 310$; the black dashed line corresponds to the shock front. The current sheets are compressed, and the amplitude of the magnetic field is amplified across the shock wave. The separation between the compressed current sheets behind the shock wave reduces to 16 from 40. The ratio of the upstream to downstream current sheet separation corresponds to the shock compression ratio. While the upstream current sheets are stable against the tearing instability, the downstream ones are unstable since their thickness is reduced by the shock wave. The tearing instability starts from $X \sim 460$. Magnetic islands are produced due to the instability, and they grow by interacting
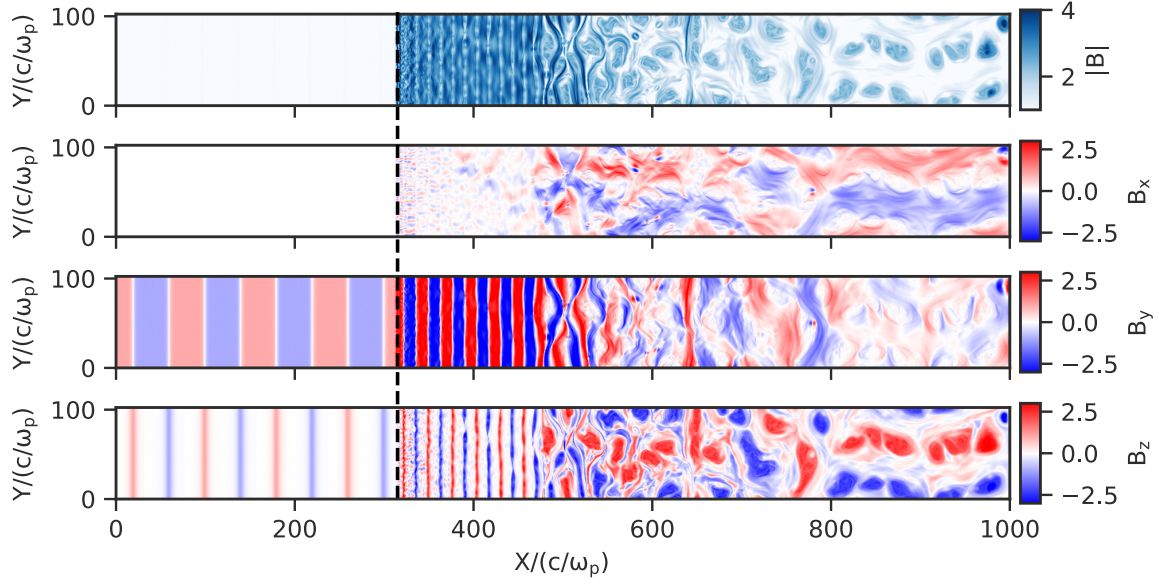
Figure 1. Snapshots of the magnitude of the magnetic field ($|B|$), and magnetic field components (B_x, B_y, B_z) from top to bottom at $T = 400$. The shock wave is located at $X \sim 310$; the black dashed line indicates the shock position. The tearing instability is initiated behind the shock of $X \sim 460$, resulting in the formation of magnetic islands thereafter.
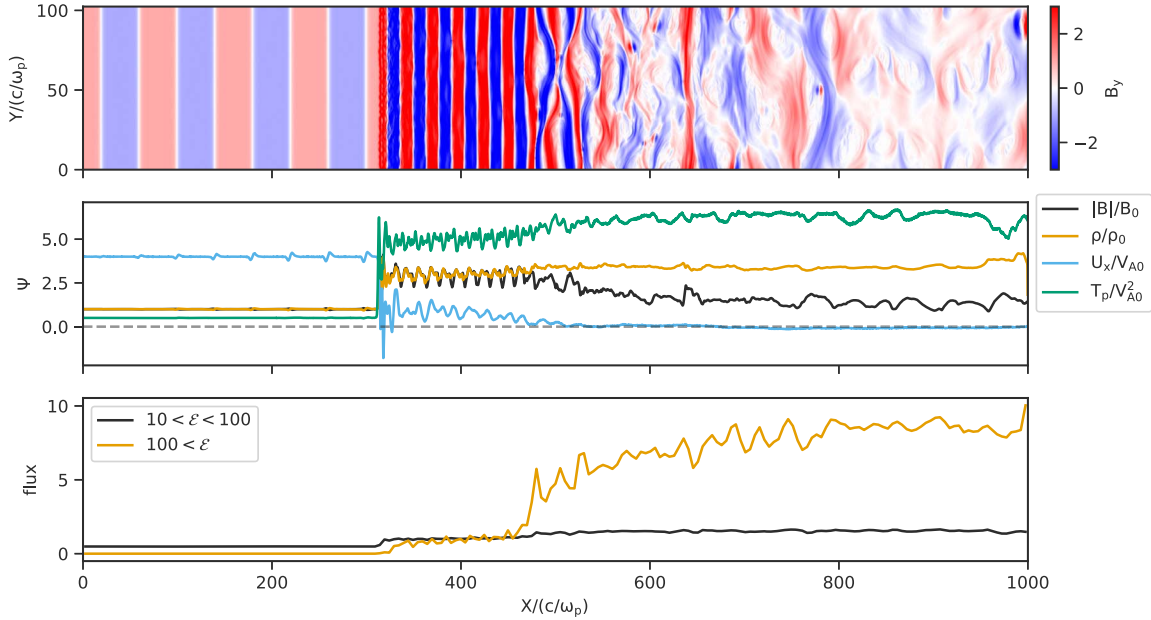

Figure 2. The top panel is the same as the B_y panel shown in Figure 1. The middle panel shows 1D profiles of the magnitude of the magnetic field (black), the plasma density (ochre), the flow speed in the x-direction (blue), and the proton temperature (green). The bottom panel shows 1D profiles of the normalized proton flux whose energy range is $10 < \mathcal{E} < 100$ (black) and $100 < \mathcal{E}$ (ochre). They are normalized by each value at $X = 400$. The time corresponds to $T = 400$.

with magnetic islands born in the next current sheet. Finally, turbulent magnetic fields develop far downstream ($X > 550$).

The interaction of multiple current sheets with a shock wave modifies the shock structure. The middle panel of Figure 2 shows a shock profile along the x-axis at $T = 400$, in which we take an average over the y-axis, for several variables: the magnitude of the magnetic field, plasma density, flow speed normal to the shock wave, and proton temperature. The upper panel of Figure 2 is the same snapshot of B_y, corresponding to that shown in Figure 1. The downstream plasma density is 2.5 times larger than the upstream density and stays constant in the downstream region (orange curve). The magnitude of the

magnetic field (black curve) and proton temperature appears to be anticorrelated. The proton temperature (green) increases from $X \sim 460$ whereas the magnitude of the magnetic field decreases. The interpretation is that some of the magnetic energy is converted into heating of the protons due to the tearing instability. The flow speed normal to the shock wave, U_x, is decelerated to 1 immediately behind the shock and then gradually decelerates to 0 at $X \sim 460$, corresponding to the evolution of the tearing instability of the current sheets downstream. Since the frame of this simulation is the downstream rest frame, the flow speed must decrease to 0 immediately behind the shock wave for a pristine upstream flow (without current sheets). We have confirmed that this is
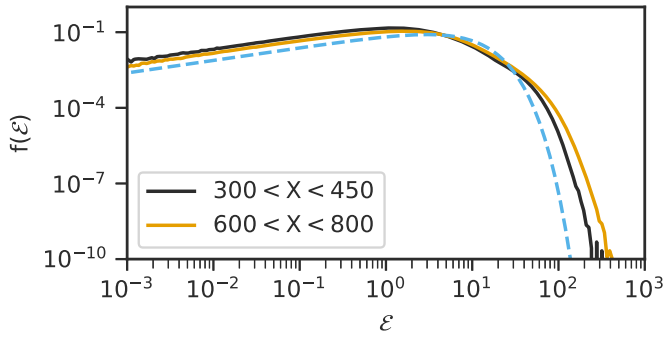
Figure 3. Proton energy spectra at $T = 400$. Black and ochre lines correspond to the region, $300 < X < 450$ and $600 < X < 800$, respectively. The dashed blue line is a Maxwellian distribution with a normalized proton temperature of 6.

the case without current sheets in our code (not shown here). This implies that the compression of current sheets removes momentum normal to the shock wave during an interaction with the shock wave, while the subsequent release occurs via the tearing instability further downstream of the shock wave. Although a detailed investigation of this feature is left for future study, this can be understood as the interaction of a shock wave with turbulence by regarding a current sheet as the sum of waves (Zank et al. 2021).

The tearing instability of current sheets downstream contributes to particle energization. The black and ochre lines in the bottom panel of Figure 2 illustrate the proton flux normalized by the value at $X = 400$ over the energy ranges $10 < \mathcal{E} < 100$ and $100 < \mathcal{E}$, respectively. At the shock front ($X \sim 310$), the fluxes increase because some ions reflect off the shock front due to the shock potential and gain energy from the upstream motional electric field. The lower-energy flux (black line) remains constant downstream. On the other hand, the higher-energy flux (ochre line) is further enhanced from $X = 460$, which is roughly consistent with the onset of the tearing instability and continues to increase up to eight times the nominal value. Figure 3 shows normalized proton energy spectra for the regions $300 < X < 450$ and $600 < X < 800$, respectively. The dashed line is a Maxwellian distribution with a proton temperature of 6 corresponding to the observed downstream temperature. Nonthermal protons are evident from $\mathcal{E} = 100$ for both spectra. The spectrum for $600 < X < 800$ (ochre line) contains more energetic protons with $\mathcal{E} > 100$ than that for $300 < X < 450$. This feature reflects the proton flux shown in the bottom panel of Figure 2, where we can see that the energization due to the tearing instability takes place, at least, over a range of $100 < \mathcal{E} < 400$. We confirmed that the extra energization downstream of the shock was also observed at earlier times (not shown here). Therefore, we can conclude that the extra energization is not due to a nonphysical effect (e.g., numerical heating), but the tearing instability of the compressed current sheets.

Figure 4 shows the trajectory of a typically accelerated particle whose energy exceeds 100 at the end of the simulation. The top panel is the time series of the particle energy. The particle is initially accelerated up to $\mathcal{E} \sim 60$ in the shock front at around $T = 150$ and then further accelerated by magnetic reconnection of the compressed current sheets downstream around $230 < T < 300$. There are two types of acceleration mechanisms during the second acceleration phase. The first type is the meandering/Speiser acceleration, which is a rapid

acceleration. This is drawn in the middle panel for $245 < T < 250$ and corresponds to the first shaded area in the top panel. The color map shows a snapshot of B_z in gray-scale color, and the color of the particle trajectory indicates the particle energy. The particle moves along a reconnected current sheet and gains energy along the z-direction due to the meandering motion. The same acceleration process is seen at an earlier time, $T = 230$. The second type is a more stochastic and gradual acceleration process and appears to be diffusive, and is illustrated in the bottom panel for $270 < T < 285$ (the second shaded area in the top panel). The particle moves in turbulent magnetic fields/magnetic islands that are fully developed from the tearing instability and is accelerated by turbulence-induced electric fields, which are generated by a coalescence of magnetic islands. This can be related to particle energization observed in full PIC simulations (Hoshino 2012; Matsumoto et al. 2015) and described theoretically as a diffusive first-order Fermi acceleration process by Zank et al. (2014) and le Roux et al. (2015).

4. Summary

We have performed 2D hybrid kinetic simulations to investigate the interaction of multiple current sheets and a shock wave. The current sheets are stable upstream and become unstable due to the tearing instability after being compressed by the shock wave. The instability generates turbulence well downstream from the shock wave via magnetic reconnection at the compressed current sheets.

We find that the interaction between current sheets and a shock wave produces a "post-cursor" region immediately behind the shock wave where the flow speed normal to the shock wave (U_x) is slowed down to $\sim 1V_A$. The flow speed is then gradually decelerated to 0, corresponding to the development of the tearing instability. Physically, the post-cursor region can be due to the current sheet compression removing momentum normal to the shock wave after their interaction, which is then subsequently released by the tearing instability.

Particle acceleration is an important aspect of the shock–current sheets interaction. There are two primary acceleration sites: (1) at the shock front, and (2) in the downstream turbulence due to the tearing instability. Some particles are reflected at the shock front and gain energy from the motional electric field. These accelerated particles can further be energized by the turbulence produced by the tearing instability of the compressed current sheets. As shown in the normalized flux of Figure 2, the second acceleration contributes to a significant energy gain for these pre-accelerated protons. This corresponds to the theoretical model developed by Zank et al. (2015). Observations find that energetic particles are efficiently accelerated by magnetic islands behind a shock wave (Zhao et al. 2018, 2019b, 2019a).

Our simulation results provide useful insight into the observed ACR enhancement behind and within 1 au of the HTS within 1 au due to magnetic islands that developed downstream (Zank et al. 2015; Zhao et al. 2018, 2019b). As can be seen in Figure 5 of Zhao et al. (2019b), the theoretical model does not fit well to the observed ACR intensities immediately behind the HTS, especially for lower-energy particles. However, the observed intensity increase begins some distance downstream of the shock wave. Our simulation results verify that this is because the onset of the tearing instability takes place some time after the upstream current sheets are compressed by the shock wave. Hence, the
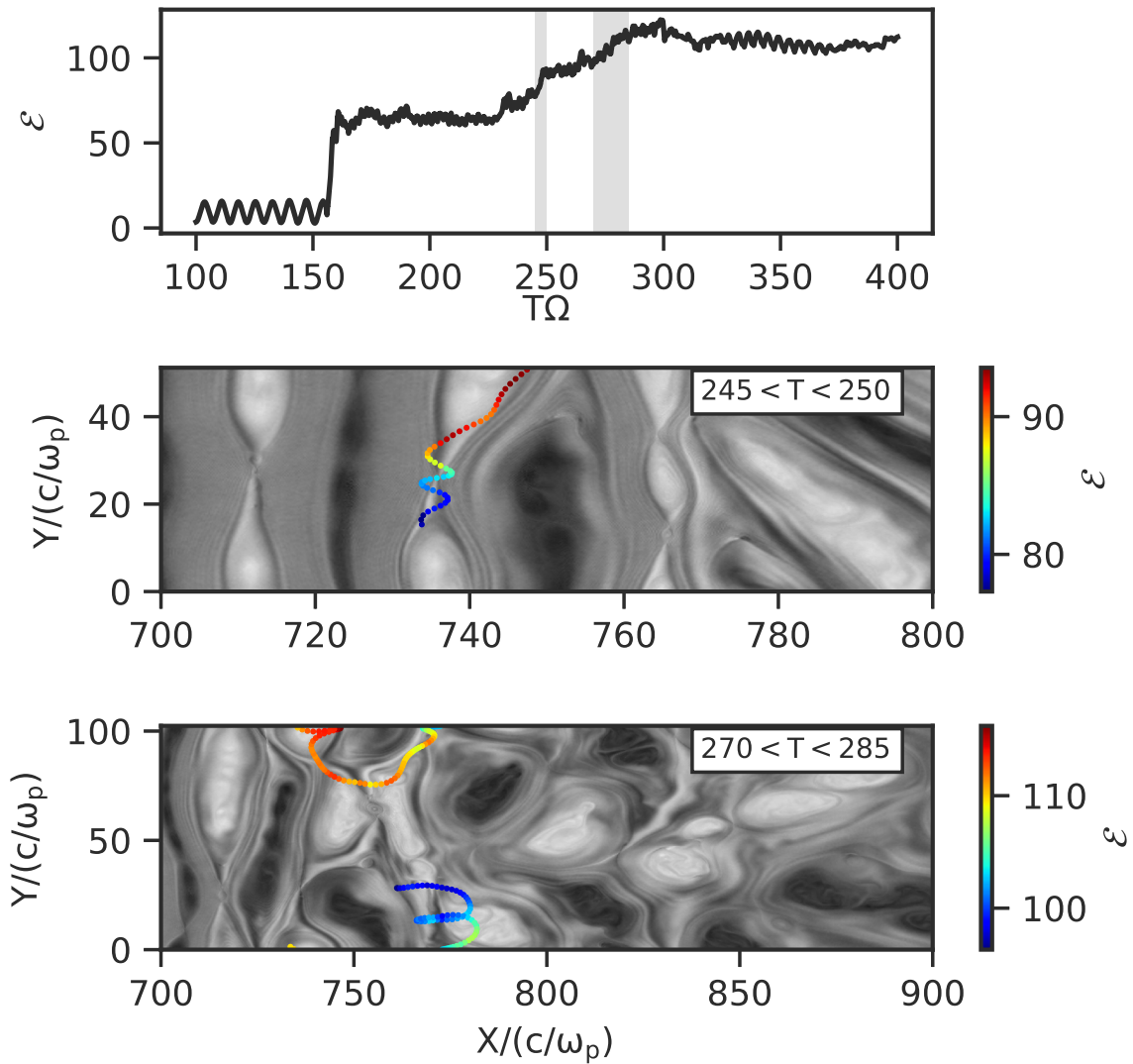
Figure 4. Typical trajectory of an accelerated proton whose energy exceeds 100. Top panel: time-series of the particle energy. The particle encounters the shock wave at around $T = 150$ and then remains downstream. Middle and bottom panels: snapshot of B_z (gray-scaled color map) at $T = 247$ and 275 and the trajectory of the particle from $T = 245$–250 and 270–285, respectively. The trajectory color corresponds to the particle energy. The times corresponding to the middle and bottom panels are indicated by the shaded areas in the top panel.

corresponding development of magnetic islands can be seen some distance behind the shock front. Therefore, the subsequent particle energization due to magnetic islands also begins some distance downstream from the shock wave, as observed by the Voyager spacecraft.

We expect some parameter dependence of the results. A larger current sheet separation will yield larger-scale magnetic islands downstream of a shock wave since magnetic islands can grow until they interact with others in adjacent current sheets. The current sheet width might affect the distance for the onset of the tearing instability from the shock front. The Mach number effectively changes the compression ratio of a shock wave, and the compressed width and separation of the current sheets is determined only by the compression ratio. Since the compression ratio is limited to 4 for a nonrelativistic shock wave, the compression of a current sheet is also limited. Although there is no significant dependency of the plasma beta on the tearing instability (Landi et al. 2008), the plasma beta drastically changes the transition region of a shock wave (Scholer et al. 2003). In the case of a low-beta plasma, the interaction of shock wave and current sheets might be expected

to become much more complicated due to an effective wave excitation at the shock-transition region, e.g., the Buneman instability and the modified two-stream instability (Matsukiyo & Scholer 2003).

Another important parameter is the angle between a current sheet and the shock normal. The study presented here focuses on the perpendicular shock case. For an oblique shock, i.e., one in which the magnetic field makes an oblique angle with respect to the shock normal, the results may change quite significantly. In this case, some particles can reflect off the shock front and propagate upstream along the magnetic field. These reflected particles possess free energy that can be released through plasma instabilities, which produce waves (Burgess & Scholer 2013). These waves might destabilize current sheets upstream of the shock wave, resulting in a very and likely highly turbulent complicated system.

It is worth noting how extending the current 2D simulation to a 3D simulation might affect the results. In the 3D case, a drift-kink instability for current sheets appears along the z-direction. Although the drift-kink instability can suppress the tearing instability according to Gingell et al. (2015),

Burgess et al. (2016a) confirmed that turbulence can still result from multiple current sheets using 3D hybrid kinetic simulations. A 3D turbulent field could be favorable for particle energization since this increases the number of possible encounters between particles and reconnection sites (Drake et al. 2003; Guo et al. 2014; Dahlin et al. 2015, 2017; Li et al. 2019). The extension to 3D might also affect the shock structure itself. For instance, Burgess et al. (2016b) carried out 3D hybrid kinetic simulations for perpendicular shock waves and found that the shock-transition region results in a coupling of the fluctuations parallel to the field (the shock rippling) and fluctuations associated with reflected ions. This results in less temperature anisotropy downstream of the shock wave.

ORCID iDs

M. Nakanotani ⬤ https://orcid.org/0000-0002-7203-0730
G. P. Zank ⬤ https://orcid.org/0000-0002-4642-6192
L.-L. Zhao ⬤ https://orcid.org/0000-0002-4299-0490

References

Adhikari, L., Khabarova, O., Zank, G. P., & Zhao, L. L. 2019, ApJ, 873, 72
Biskamp, D. 1986, PhFl, 29, 1520
Biskamp, D. 1996, Ap&SS, 242, 165
Bobrova, N. A., Bulanov, S. V., Sakai, J. I., & Sugiyama, D. 2001, PhPl, 8, 759
Burgess, D., Gingell, P. W., & Matteini, L. 2016a, ApJ, 822, 38
Burgess, D., Hellinger, P., Gingell, I., & Trávníček, P. M. 2016b, JPlPh, 82, 905820401
Burgess, D., & Scholer, M. 2013, SSRv, 178, 513
Cummings, A. C., & Stone, E. C. 2013, in AIP Conf. Ser. 1516, Centenary Symp. 2012: Discovery of Cosmic Rays, ed. J. F. Ormes (Melville, NY: AIP), 97
Dahlin, J. T., Drake, J. F., & Swisdak, M. 2015, PhPl, 22, 100704
Dahlin, J. T., Drake, J. F., & Swisdak, M. 2017, PhPl, 24, 092110
Decker, R. B., Krimigis, S. M., Roelof, E. C., et al. 2005, Sci, 309, 2020
Drake, J. F., Opher, M., Swisdak, M., & Chamoun, J. N. 2010, ApJ, 709, 963
Drake, J. F., Swisdak, M., Cattell, C., et al. 2003, Sci, 299, 873
Drake, J. F., Swisdak, M., Che, H., & Shay, M. A. 2006, Natur, 443, 553
Du, S., Guo, F., Zank, G. P., Li, X., & Stanier, A. 2018, ApJ, 867, 16
Du, S., Zank, G. P., Li, X., & Guo, F. 2020, PhRvE, 101, 033208
Fan, F., Huang, C., Lu, Q., Xie, J., & Wang, S. 2016, PhPl, 23, 112106
Giacalone, J., & Burgess, D. 2010, GeoRL, 37, L19104
Giacalone, J., & Ellison, D. C. 2000, JGR, 105, 12541
Giacalone, J., Nakanotani, M., Zank, G. P., et al. 2021, ApJ, 911, 27
Gingell, I., Sorriso-Valvo, L., Burgess, D., De Vita, G., & Matteini, L. 2017, JPlPh, 83, 705830104
Gingell, P. W., Burgess, D., & Matteini, L. 2015, ApJ, 802, 4
Guo, F., Giacalone, J., & Zhao, L. 2021, FrASS, 8, 27
Guo, F., Li, H., Daughton, W., & Liu, Y.-H. 2014, PhRvL, 113, 155005
Hoshino, M. 2012, PhRvL, 108, 135003
Landi, S., Londrillo, P., Velli, M., & Bettarini, L. 2008, PhPl, 15, 012302
Lavraud, B., Fargette, N., Réville, V., et al. 2020, ApJL, 894, L19
Le, A., Daughton, W., Karimabadi, H., & Egedal, J. 2016, PhPl, 23, 032114
le Roux, J. A., Zank, G. P., Webb, G. M., & Khabarova, O. 2015, ApJ, 801, 112
le Roux, J. A., Zank, G. P., Webb, G. M., & Khabarova, O. V. 2016, ApJ, 827, 47
Li, X., Guo, F., Li, H., Stanier, A., & Kilian, P. 2019, ApJ, 884, 118
Lu, Y., Guo, F., Kilian, P., et al. 2021, ApJ, 908, 147
Lyubarsky, Y. 2005, AdSpR, 35, 1112
Matsukiyo, S., & Scholer, M. 2003, JGRA, 108, 1459
Matsumoto, M., Kajimura, Y., Usui, H., Funaki, I., & Shinohara, I. 2012, CoPhC, 183, 2027
Matsumoto, Y., Amano, T., Kato, T. N., & Hoshino, M. 2015, Sci, 347, 974
Matthews, A. P. 1994, JCoPh, 112, 102
McComas, D. J., & Schwadron, N. A. 2006, GeoRL, 33, L04102
Nagata, K., Hoshino, M., Jaroschek, C. H., & Takabe, H. 2008, ApJ, 680, 627
Nakanotani, M., Zank, G. P., & Zhao, L. 2020, JPhCS, 1620, 012014
Nishimura, K., Gary, S. P., Li, H., & Colgate, S. A. 2003, PhPl, 10, 347
Oka, M., Phan, T. D., Krucker, S., Fujimoto, M., & Shinohara, I. 2010, ApJ, 714, 915
Richardson, J. D., Burlaga, L. F., Drake, J. F., Hill, M. E., & Opher, M. 2016, ApJ, 831, 115
Schoeffler, K. M., Drake, J. F., & Swisdak, M. 2011, ApJ, 743, 70
Scholer, M., Shinohara, I., & Matsukiyo, S. 2003, JGRA, 108, 1014
Sironi, L., & Spitkovsky, A. 2011, ApJ, 741, 39
Stone, E. C., Cummings, A. C., McDonald, F. B., et al. 2005, Sci, 309, 2017
Stone, E. C., Cummings, A. C., McDonald, F. B., et al. 2008, Natur, 454, 71
Su, Y., Lu, Q., Huang, C., et al. 2012, JGRA, 117, A08107
Trotta, D., Valentini, F., Burgess, D., & Servidio, S. 2021, PNAS, 118, 2026764118
Tsubouchi, K., & Matsumoto, H. 2005, JGRA, 110, A04101
Winske, D., & Omidi, N. 1996, JGR, 101, 17287
Zank, G. P., Hunana, P., Mostafavi, P., et al. 2015, ApJ, 814, 137
Zank, G. P., le Roux, J. A., Webb, G. M., Dosch, A., & Khabarova, O. 2014, ApJ, 797, 28
Zank, G. P., Nakanotani, M., Zhao, L. L., et al. 2021, ApJ, 913, 127
Zhao, L. L., Zank, G. P., Chen, Y., et al. 2019a, ApJ, 872, 4
Zhao, L. L., Zank, G. P., Hu, Q., et al. 2019b, ApJ, 886, 144
Zhao, L.-L., Zank, G. P., Khabarova, O., et al. 2018, ApJL, 864, L34